J Eng Math: (2021) 129:10
https://doi.org/10.1007/s10665-021-10150-2

Resonant mode scanning to compute the spectrum of capillary surfaces with dynamic wetting effects

Joshua McCraney · **Joshua Bostwick** ·
Paul Steen

Received: 4 March 2021 / Accepted: 12 June 2021

Abstract A capillary surface bound by a solid rectangular channel exhibits dynamic wetting effects characterized by a constitutive law relating the dynamic contact-angle to the contact-line speed through the contact-line mobility Λ parameter. Limiting cases correspond to the free ($\Lambda = 0$) and pinned ($\Lambda = \infty$) contact-line. Viscous potential flow is used to derive the governing integrodifferential equation from a boundary integral approach. The spectrum is determined from a boundary value problem where the eigenvalue parameter appears in the boundary condition. Here we introduce a new frequency scan approach to compute the spectrum, whereby we scan the complex frequency plane and compute the system response from which we identify the complex resonant frequency. Damping effects due to viscosity and Davis dissipation from finite Λ do not attenuate signal response, but rather shift the response poles into the complex plane. Our new approach is verified against an analytical solution in the appropriate limit. We identify the critical mobility that maximizes Davis dissipation and the critical Ohnesorge number (viscosity) where the transition from underdamped to overdamped oscillations occurs, as it depends upon the static contact-angle α. Our approach is applied to a rectangular channel, but is suitable for a myriad of geometric supports.

Keywords Capillary waves · Contact lines · Eigenvalue problem · Integrodifferential equation

1 Introduction

Liquids mechanically driven into resonance by plane-normal forcing of the base substrate exhibit oscillations of the bounding liquid/gas interface. The resonant frequencies and interfacial mode shapes are affected by the wetting properties of the solid substrate through the static contact-angle α and mobility of the contact-line (CL). Disturbances

J. McCraney and P. Steen acknowledge support from NASA Grant NNH17ZTT001N-17PSI D. J. Bostwick acknowledges support from NSF Grants CMMI-1935590.

J. McCraney (✉)
School of Mechanical and Aerospace Engineering, Cornell University, Ithaca, NY, USA
e-mail: jm2555@cornell.edu

J. Bostwick
Department of Mechanical Engineering, Clemson University, Clemson, SC, USA
e-mail: jbostwi@clemson.edu

P. Steen
School of Chemical and Biomolecular Engineering, Cornell University, Ithaca, NY, USA

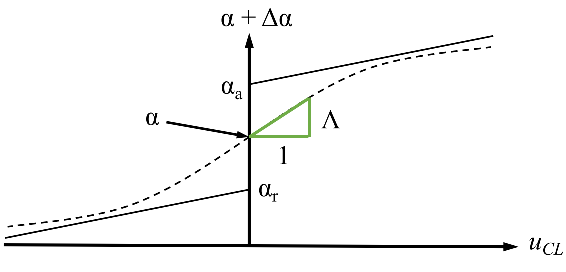

Fig. 1 Dynamic contact-line (CL) law relating the contact-angle $\alpha + \Delta\alpha$ to the CL speed $u_{\rm CL}$ with (solid) and without (dashed) hysteresis. Here, α_a and α_r are the advancing and receding static contact-angles ($u_{\rm CL} \to 0$), respectively

to the interface displace the CL, though for the CL to move it must appear to violate the no-slip condition. This quandary has lead to the empirical development of numerous dynamic CL models [1–5], including the CL models by Bracke [6,7] and Kistler [8,9]. Saha and Mitra [10] compare many of the aforementioned models in 3D microfluidic channel simulations. Here we model the CL via the Hocking condition [11], originally introduced by Davis [12], which assumes the CL dynamics obey the general CL law relating the linearized deviation in contact-angle $\Delta\alpha$ from its static value α to the CL speed $u_{\rm CL}$ depicted in Fig. 1:

$$\Delta\alpha = \Lambda u_{\rm CL}. \tag{1}$$

Positive (negative) $U_{\rm CL}$ implies liquid displaces gas (gas displaces liquid), which is controlled through the homotopy parameter $\Lambda \in [0, \infty)$. The limit $\Lambda = 0$ implies a free CL (constant contact-angle) and $\Lambda = \infty$ implies a pinned CL. Rare space experiments of surface tension-dominated flows have been analyzed and numerically reported for free CLs in wedge geometries [13] as well as pinned CLs for cylindrical support geometries [14,15]. Here we consider non-limiting Λ, where the system undergoes damping from the CL, even if the liquid is inviscid, and this has come to be known as Davis dissipation [12,16,17]. While other approaches model viscosity directly through stress balances [18,19], here we analyze viscous dissipation through viscous potential flow [20,21] and CL damping from Λ. More complicated models incorporating CL hysteresis [22] are incompatible with the linear analysis of this work [12].

In low-g environments and micro-terrestrial systems, geometric support influences the fundamental frequencies of liquids such as droplets [16,23] and rivulets [24] on planar substrates, belt supports [25], pinned circle of contacts [26], toroidal supports [27], spherical bowl supports [28], and bubbles within containers [29]. Herein we consider liquid partially filling a rectangular channel, Fig. 2. The hydrodynamic equations associated with small disturbances to the fluid interface compose a differential eigenvalue problem with unusual differential structure: the interfacial boundary condition is of higher differential order than the governing partial differential equation. Several solution methods exist to address the pinned CL including a variational approach using a Lagrange multiplier [30,31], the introduction of a singular pressure at the CL [32], and a Rayleigh–Ritz minimization procedure over a constrained function space [25,33]. We use the latter approach in our theoretical development. In this manner, the differential eigenvalue problem can be reduced to an algebraic eigenvalue problem with similar structure to a damped harmonic oscillator

$$M + \mathrm{i}\lambda\tau + \lambda^2 K = 0. \tag{2}$$

Here M is a positive definite matrix representing channel inertia (mass), K is a matrix representing capillarity (spring constant), and τ is a matrix representing bulk viscosity. Equation (2) is typically solved via an eigenvalue Rayleigh–Ritz method [16,24,27], where the CL is assumed free or pinned ($\Lambda = 0, \infty$). A comprehensive review of the technique is outlined by Bostwick and Steen [17]. However, non-limiting mobility values imply the eigenvalue λ appears in the CL boundary condition associated with (2), and the method fails. We subvert this complication by

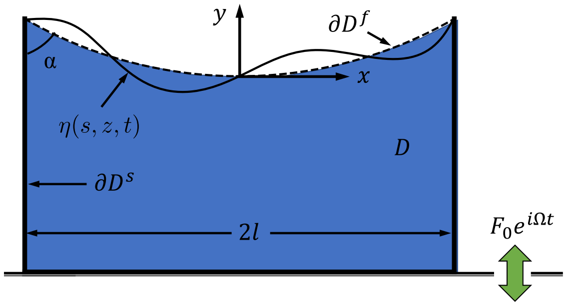

Fig. 2 Definition sketch illustrating the perturbed free surface driven by sinusoidal pressure $p = F_0 e^{i\Omega t}$ of amplitude F_0 and frequency Ω

introducing forcing through channel bulk pressure via a pressure field [34], structurally changing (2) to

$$M + i\omega\tau + \omega^2 K = \omega F, \tag{3}$$

where F is a forcing vector at frequency ω. With ω an input parameter, (3) is reduced from an algebraic eigenvalue problem to a linear system of equations, from which the system response can be determined from the frequency response diagram. Recent frequency scan implementations assume $\omega \in \mathbb{R}$, thereby only resolving oscillatory modes [35,36]. We introduce a new computational technique by scanning the entire complex plane $\omega \in \mathbb{C}$ resolving the complex spectrum through identification of resonance peaks in the complex frequency plane. This technique involves solving a linear system as opposed to an eigenvalue problem, and thus is computationally efficient for fundamentals with small damping modes (all results shown herein). However, since we scan the entire complex plane, as opposed to only the real number line, the computations can become expensive, which one can mitigate by preselecting a neighborhood near resonance. This is especially true for modes with large damping, i.e., maximal Davis dissipation. Nevertheless, the proposed approach is computationally cheaper than full CFD simulations. We verify the computational approach on the limiting case with analytical solution. The utility of the procedure is that it resolves all dissipative characteristics and is computationally efficient and robust.

2 Mathematical formulation

Consider an incompressible fluid with density ρ and viscosity μ that is subject to a time-dependent pressure field $p(t) = P_0 e^{i\Omega t}$. The fluid occupies domain D bounded by a liquid–gas interface ∂D^{f} with surface tension σ in a rectangular channel ∂D^{s} with half-width l, shown in Fig. 2. The equilibrium surface is defined parametrically as

$$X(s;\alpha) = \frac{\sin(s\cos\alpha)}{\cos\alpha}, \qquad Y(s;\alpha) = \frac{1-\cos(s\cos\alpha)}{\cos\alpha}, \qquad Z(z) = z, \tag{4}$$

using $s \in [-s_0(\alpha), s_0(\alpha)]$ and $z \in [-\infty, \infty]$ as generalized surface coordinates, with equilibrium contact-angle α. Here s_0 and the cross-sectional liquid area A are calculated as

$$s_0 = \frac{\arcsin(\cos\alpha)}{\cos\alpha}, \quad \frac{A}{2} = h + \int_0^{s_0} Y(s)X'(s)\,\mathrm{d}s, \tag{5}$$

where $h > 0$ is the center $(x = 0)$ channel depth. Gravitational effects have been neglected. The interface is given a small perturbation $\eta(s, z, t)$. No domain perturbation is necessary for linear problems.

2.1 Field equations

The velocity field $\boldsymbol{u} = -\nabla\Psi$ for this interfacial-driven flow can be expressed using the velocity potential Ψ. The potential Ψ satisfies the following Neumann boundary value problem,

$$\nabla^2\Psi = 0[D], \qquad \nabla\Psi \cdot \hat{n} = 0[\partial D^{\mathrm{s}}], \qquad \Psi_n = -\eta_t[\partial D^{\mathrm{f}}], \tag{6}$$

where $\hat{n}$ is the unit outward normal vector to the prescribed surface and subscripts denote partial derivatives with respect to that independent variable. The inertial pressure field is given by the unsteady linearized Bernoulli equation

$$p = \rho\Psi_t + P_0 \mathrm{e}^{\mathrm{i}\Omega t}[D]. \tag{7}$$

The normal stress balance at the interface ∂D^{f} is given by the Young–Laplace equation

$$p - \mu\hat{n} \cdot (\nabla \otimes \nabla\Psi) \cdot \hat{n} = -\sigma\left(\left(\kappa_1^2 + \kappa_2^2\right)\eta + \Delta_{\partial D^{\mathrm{f}}}\eta\right)[\partial D^{\mathrm{f}}], \tag{8}$$

where $\kappa_{1,2}$ are the principal curvatures. Note the potential flow assumption made here assumes that no-slip condition cannot be satisfied on ∂D^{s}, yet viscosity μ enters the equations through the normal stress balance. This is what is described as viscous potential flow (VPF) [34]. The Laplace–Beltrami operator $\Delta_{\partial D^{\mathrm{f}}}$, or surface Laplacian, is defined as [37]

$$\Delta_{\partial D^{\mathrm{f}}}\eta \equiv \frac{1}{\sqrt{g}}\frac{\partial}{\partial u^\mu}\left(\sqrt{g}g^{\mu\nu}\frac{\partial\eta}{\partial u^\nu}\right) \tag{9}$$

(summation notation implied) with the surface metric $g_{\mu\nu} \equiv \partial_\mu\boldsymbol{x} \cdot \partial_\nu\boldsymbol{x}$, $g = 1$ acting on surface coordinates $\mu, \nu = 1, 2$. The CL dynamics obey the contact-line speed law (Appendix A from Bostwick and Steen [16])

$$\partial_s\eta(s_0) + \cot\alpha\cos\alpha\,\eta(s_0) = -\Lambda\Psi_n(s_0). \tag{10}$$

Equations (6)–(10) together compose the hydrodynamic equations of motion for a small disturbance in the absence of gravity.

2.2 Normal mode reduction

Variables are non-dimensionalized with the vessel half-width l

$$\bar{\eta} = \eta/l, \quad \bar{t} = t\Big/\sqrt{\frac{\rho l^3}{\sigma}}, \quad \bar{\Psi} = \Psi\Big/\sqrt{\frac{\sigma l}{\rho}}, \quad \bar{p} = p\Big/\frac{\sigma}{l} \tag{11}$$

and we drop the overbars hereafter with the understanding that all variables are dimensionless. Normal modes are assumed via the scaled temporal frequency $\omega \equiv \Omega\sqrt{\rho l^3/\sigma}$ and axial wave-number ξ,

$$\Psi(x, y, z, t) = \phi(x, y)\mathrm{e}^{\mathrm{i}\omega t}\mathrm{e}^{\mathrm{i}\xi z}, \quad \eta(x, y, z, t) = \psi(x, y)\mathrm{e}^{\mathrm{i}\omega t}\mathrm{e}^{\mathrm{i}\xi z} \tag{12}$$

and substituted into (6)–(10) to yield the boundary value problem for the potential ϕ:

$$\nabla^2\phi = 0[D], \tag{13a}$$

$$\phi_n = 0[\partial D^{\mathrm{s}}], \tag{13b}$$

$$\int_0^{s_0} \phi_n \, \mathrm{d}s = 0[\partial D^{\mathrm{f}}], \tag{13c}$$

$$\phi_n' + \cos\alpha \cot\alpha \phi_n = \mathrm{i}\omega\Lambda\phi_n[\partial D^{\mathrm{f}} \cap \partial D^{\mathrm{s}}], \tag{13d}$$

$$\omega^2\phi - \mathrm{i}\epsilon\omega\hat{n} \cdot (\nabla \otimes \nabla\phi) \cdot \hat{n} - \phi_n'' - \left(\cos^2\alpha - \xi^2\right)\phi_n = \omega F_0[\partial D^{\mathrm{f}}], \tag{13e}$$

where $\epsilon \equiv \mu/\sqrt{\rho l \sigma}$ is the Ohnesorge number and $F_0 \equiv P_0 l^2/\sigma$ the scaled forcing amplitude. Here $' = \mathrm{d}/\mathrm{d}s$ and the interface deformation η is related to ϕ_n through the kinematic condition (6).

3 Solution method

The boundary value problem (13) can be viewed as either (1) a forced oscillation problem where $F_0 \neq 0$ and ω is a known parameter or (2) a natural oscillation (or eigenvalue) problem ($F_0 = 0$) where the frequency ω is unknown and must be determined as part of the solution. For the natural oscillation problem, the presence of the eigenvalue in the boundary condition (13d) is known to lead to computational instability [38]. To resolve this issue, we introduce a new technique whereby we scan the frequency over the complex plane and identify resonances, i.e., maxima in the system response, from which we identify the complex eigenvalue.

Our solution procedure is a boundary integral approach whereby the problem is mapped to the boundary and the dynamic pressure balance there (13e) is recast as an integral equation that we apply the Ritz method to a function space which satisfies (13a)–(13d). The resulting set of algebraic equations are parameterized by the frequency ω, contact-angle α, CL mobility Λ, Ohnesorge number ϵ, and forcing amplitude F_0.

3.1 Green's function

To begin, we rewrite the dynamic pressure balance at the interface (13e) as an integral equation

$$\phi_n - \mathrm{i}\epsilon\omega \int_0^{s_0} G\hat{n} \cdot \nabla \otimes \nabla\phi \cdot \hat{n} \, \mathrm{d}s - \omega^2 \int_0^{s_0} G\phi \, \mathrm{d}s = F_0\omega \int_0^{s_0} G \, \mathrm{d}s, \tag{14}$$

using the Green's function G for the curvature operator

$$K[f](x) = -f''(x) - \left(\cos^2\alpha - \xi^2\right) f(x). \tag{15}$$

Solutions can be decomposed according to their symmetry about the symmetry plane $x = 0$ into odd

$$f(0) = 0 \tag{16}$$

and even

$$f'(0) = 0 \tag{17}$$

extensions. These are combined with the dynamic CL condition

$$f'(s_0) + \cos\alpha \cot\alpha f(s_0) = \mathrm{i}\omega\Lambda f(s_0). \tag{18}$$

The Green's function is built via variation of parameters

$$G(x,y)=\begin{cases}-\frac{L^m(x)R(y)}{W}: 0\le x\le y\le s_0,\\ -\frac{L^m(y)R(x)}{W}: 0\le y\le x\le s_0,\end{cases} \tag{19}$$

where superscripts $m=\{o,e\}$ denote odd or even symmetry conditions, respectively. Here the left-hand solution L satisfies boundary condition (16) or (17),

$$L^{\mathrm{o}}(x)=\sin\left(\sqrt{\cos\alpha-\xi^2}x\right),\qquad L^{\mathrm{e}}(x)=\cos\left(\sqrt{\cos\alpha-\xi^2}x\right), \tag{20}$$

the right-hand solution R satisfies boundary condition (18)

$$R(x)=\sqrt{\cos^2\alpha-\xi^2}\cos\left((s_0-x)\sqrt{\cos^2\alpha-\xi^2}\right)+(\cos\alpha\cot\alpha-\mathrm{i}\omega\Lambda)\sin\left((s_0-x)\sqrt{\cos^2\alpha-\xi^2}\right). \tag{21}$$

The Wronskian W is determined via standard techniques.

3.2 Volume conservation constraint

Symmetry arguments can be used to show that odd solutions naturally satisfy the volume conservation condition [39]. For the even problem, we can modify the integral form of the dynamic pressure balance [16] by introducing a constant term C to the velocity potential ϕ,

$$\phi_n-\mathrm{i}\epsilon\omega\int_0^{s_0}G\hat{n}\cdot\nabla\otimes\nabla\phi\cdot\hat{n}\,\mathrm{d}s-\omega^2\int_0^{s_0}G\phi\,\mathrm{d}s=\omega^2C\int_0^{s_0}G\,\mathrm{d}s. \tag{22}$$

Here we have set $F_0=0$ without loss of generality since forced vibrations do not affect volume conservation. Integrating (22) over ∂D^{f} and enforcing the volume conservation constraint (13c) yields an expression for C

$$C=-\frac{\mathrm{i}\epsilon\int_0^{s_0}\int_0^{s_0}G\hat{n}\cdot\nabla\otimes\nabla\phi\cdot\hat{n}\,\mathrm{d}x\,\mathrm{d}y+\omega\int_0^{s_0}\int_0^{s_0}G\phi\,\mathrm{d}x\,\mathrm{d}y}{\int_0^{s_0}\int_0^{s_0}G\,\mathrm{d}x\,\mathrm{d}y}. \tag{23}$$

We can then write the even extension of the dynamic pressure balance as

$$\phi_n-\mathrm{i}\epsilon\omega\int_0^{s_0}G\hat{n}\cdot\nabla\otimes\nabla\phi\cdot\hat{n}\,\mathrm{d}s-\omega^2\int_0^{s_0}(\phi+C)\,\mathrm{d}s=F_0\omega\int_0^{s_0}G\,\mathrm{d}s. \tag{24}$$

3.3 Reduction to matrix equation

A solution is constructed from basis functions ϕ_j, where

$$\Phi=\sum_{j=1}^{N}a_j\phi_j \tag{25}$$

is applied to the odd (14) and even (24) problems, and inner products are taken to generate a set of algebraic equations

$$\sum_{j=1}^{N}\left(m_{ij}-\mathrm{i}\epsilon\omega\tau_{ij}-\omega^2k_{ij}\right)a_j=F_0\omega\gamma_i, \tag{26}$$

where

$$m_{ij} \equiv \int_0^{s_0} \phi_{n\,i}(x)\phi_j(x)\,\mathrm{d}x, \tag{27a}$$

$$k_{ij} \equiv \int_0^{s_0}\int_0^{s_0} G\phi_i(x)\phi_j(y)\,\mathrm{d}x\,\mathrm{d}y, \tag{27b}$$

$$\tau_{ij} \equiv \int_0^{s_0}\int_0^{s_0} G\left(\hat{n}\cdot\nabla\otimes\nabla\phi_i(x)\cdot\hat{n}\right)\phi_j(y)\,\mathrm{d}x\,\mathrm{d}y, \tag{27c}$$

$$\gamma_i \equiv \int_0^{s_0}\int_0^{s_0} G\phi_i(x)\,\mathrm{d}x\,\mathrm{d}y. \tag{27d}$$

Here the unit normal $\hat{n}$ to ∂D^{f} is given by

$$\hat{n} = \frac{\langle -Y'(s), X'(s), 0\rangle}{\sqrt{Y'(s)^2 + X'(s)^2}}. \tag{28}$$

We normalize the basis functions such that $m_{ii} = 1$

$$\phi_j = c_j\psi_j,\; c_j = \left(\int_0^{s_0} \psi_j\ \psi_{n\,j}\ \mathrm{d}s\right)^{-1/2}. \tag{29}$$

The basis functions ψ_j are the analytic solutions to (13) for $\alpha = 90°$, $\Lambda = 0$, $\epsilon = 0$, and are decomposed according to their symmetry

$$\psi_j^o = \sin(\mu_j^o x)\cosh\left((y+h)\sqrt{(\mu_j^o)^2 + \xi^2}\right), \tag{30a}$$

$$\psi_j^e = \cos(\mu_j^e x)\cosh\left((y+h)\sqrt{(\mu_j^e)^2 + \xi^2}\right), \tag{30b}$$

with associated constants

$$\mu_j^o = \pi(j - 1/2), \quad \mu_j^e = \pi j, \qquad j = 1, 2, 3\ldots. \tag{31}$$

Since ψ^o and ψ^e are Fourier modes (in x), they are complete orthogonal systems in two mutually orthogonal subspaces (odd and even) and together form a Hilbert space and are thus admissible basis functions. The natural frequencies λ_j for this special case are given by

$$\lambda_j(\xi = 0) = \frac{1}{8}\left(\sqrt{\pi^3 j^3\left(8\tanh\left(\frac{\pi h j}{2}\right) - \pi j\epsilon^2\right)} - \mathrm{i}\pi^2 j^2\epsilon\right). \tag{32}$$

4 Results

For fixed ω, Λ, ϵ, $A(h)$, α, ξ, the solution a_j to (26) is readily computed with the associated fluid response Φ, Φ_n then obtained by applying a_j to (25). Figure 3 shows typical solutions for free $\Lambda = 0$ (Fig. 3a) and pinned $\Lambda = \infty$ (Fig. 3b) CL conditions. To identify resonance frequencies for any Λ, the frequency ω is varied through $\mathbb{C}$, all other parameters held constant, and the response $|a|$ computed. The location of the peaks in the complex frequency plane

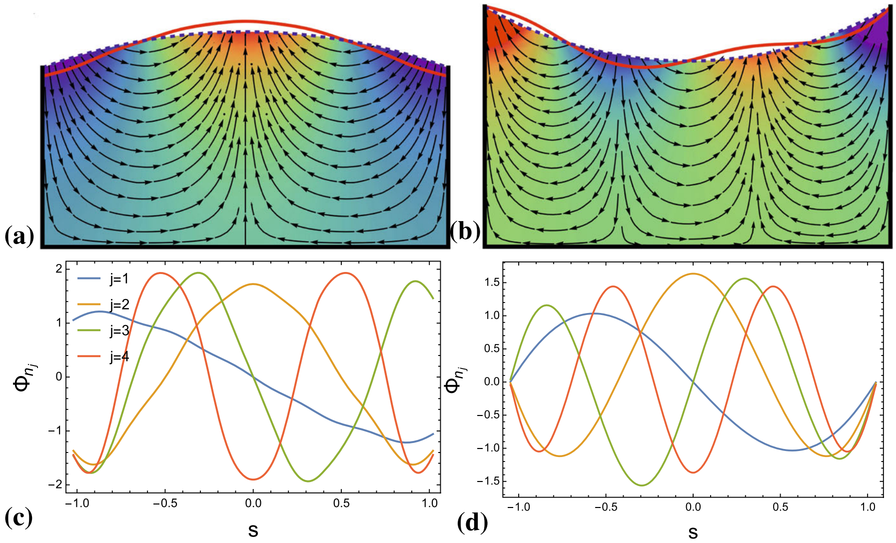

Fig. 3 Solutions for **a** $j = 2$, $\omega = 5.54$, $\alpha = 110°$, $\Lambda = 0$ and **b** $j = 3$, $\omega = 12.46$, $\alpha = 60°$, $\Lambda = \infty$. **a**, **b** The equilibrium interface (blue, dashed) is disturbed (red, solid) and streamlines (black arrows) are plotted over the scaled pressure field (color). The first four resonant modes for **c** $\Lambda = 0$, $\alpha = 110°$, $\epsilon = 0$ and **d** $\Lambda = \infty$, $\alpha = 60°$, $\epsilon = 0$. (Color figure online)

Fig. 4 Frequency response for the first two odd $j = 1, 3$ modes with $\alpha = 110°$, $\epsilon = 0$, contrasting $\Lambda = 0.1$ and $\Lambda = 0.5$, in **a** three-dimensional, **b** projected, and **c** traced in the $\mathrm{Im}(\omega) = 0$ plane

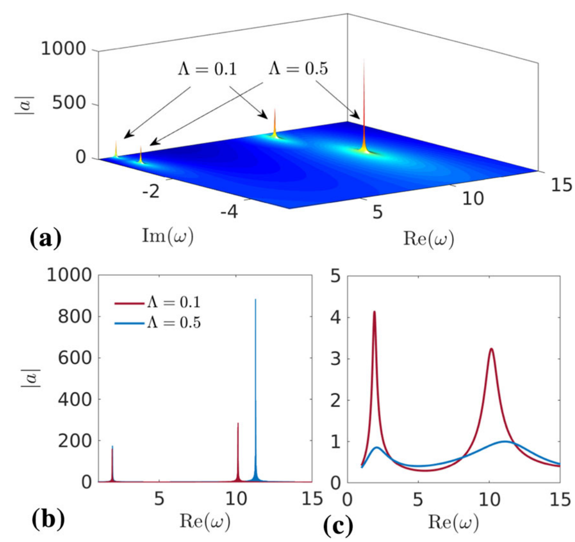

yield the resonant frequencies (complex eigenvalues). Fig 4a shows a typical system response using this approach for $\Lambda = 0.1, 0.5$. Here $\mathrm{Re}(\lambda)$ corresponds to the oscillation frequency and $\mathrm{Im}(\lambda)$ the decay rate.

In what follows, we compute the natural frequencies using our frequency scan approach focusing on the role of CL mobility Λ and viscosity ϵ. Hereafter we set $A = 2$, $\xi = 0$ and the truncation $N = 5$ which is sufficient to provide iterative convergence $< 1\%$.

4.1 CL damping

Figure 5 plots the resonant frequencies λ for an inviscid $\epsilon = 0$ fluid with hydrophobic $\alpha = 110°$ wetting conditions. The oscillation frequency $\mathrm{Re}(\lambda)$ is minimal at $\Lambda = 0$ corresponding a free CL and maximal at $\Lambda = \infty$ corresponding to a pinned CL, as shown in Fig. 5a. For finite Λ there is a small range over which the frequency increases from the

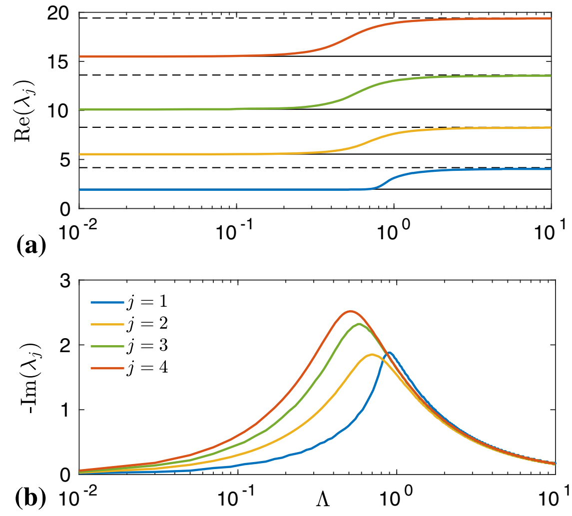

Fig. 5 Natural frequency against mobility parameter Λ plotting **a** oscillatory frequency Re(λ) and **b** decay rate Im(λ) for $\alpha = 110°, \epsilon = 0$

lower plateau (free) to higher plateau (pinned) and the width of this transition region increases with mode number j. The decay rate Im(λ) $\to 0$ in both free $\Lambda \to 0$ and pinned $\Lambda \to \infty$ limits, as shown in Fig. 5b, implies no dynamic wetting effects. However, for non-limiting Λ, CL dissipation leads to underdamped motions.

Recent frequency scan procedures scan only the real number line [35,36,40]. As such, increased dissipative effects (CL or viscous) are incorrectly reported to attenuate the signal. Signal attenuation is then incorrectly interpreted to imply increased damping. In what follows, we explain this misunderstanding. In Fig. 4 we increase the mobility from $\Lambda = 0.1$ to 0.5 for $j = 1, 3$ modes, which increases the CL damping for both modes, Fig. 5b. Figure 4c plots a frequency response for a scan of only the real number line (the Im(ω) = 0 plane), where increasing $\Lambda = 0.1$ to 0.5 appears to attenuate the signal, evidenced by the smaller peaks. However, scanning the entire complex plane (not only the real number line) and projecting response $|a|$ onto the Im(ω) = 0 plane Fig. 4b, it is clear the increased CL dissipative signals do not attenuate. Rather, the signal poles shift further into the complex plane, Fig. 4a. While the poles appear to be different heights, they are all infinite, as required by (26), though finite sampling of ω implies finite signal response $|a|$. Note shifts into the complex plane imply Im(ω) increases in magnitude, which increases system damping as implied by the temporal normal mode assumption (12). This recognition corrects the current interpretation 'increased damping attenuates signal response' to 'increased damping does not attenuate response, but shifts the response further into the complex plane.' Then signal response height $|a|$ in the Im(ω) = 0 plane is not immediately related to system damping, only an artifact of signal shifts.

Inducing damping, i.e., retarding fluid motion, can be desirable in application, such as switchable wettability in systems aboard spacecraft [41], surface wrinkles [42] found in insects, geckos, and plants [43–45], micro-structure fabrication via capillary origami [46], inkjet sprays [47], electrowetting [48], and energy harvesting via liquid metal CL motions [49]. Then identifying the mobility parameter that maximizes CL dissipation is important. Each mode shown in Fig. 5b exhibits a single maximum at a critical CL mobility Λ^*. Figure 6a shows Λ^* exhibits a single minimum near $\alpha = 90°$, which corresponds to a maximal decay rate Im(λ) as shown in Fig. 6c. Figure 6 can be used as a guide in selecting substrates with prescribed wettability that generates a desired CL dissipation.

4.2 Viscous damping

For viscous $\epsilon \neq 0$ liquids, the total dissipation is due to both viscous and CL effects. Figure 7 plots the resonant frequency λ against the CL mobility Λ, as it depends upon viscosity ϵ. Recall that in the inviscid limit $\epsilon = 0$, the oscillation frequency Re(λ) monotonically increased with Λ. Figure 7a shows a non-monotonic dependence of Re(λ) with Λ for a range of $\epsilon \neq 0$, which illustrates a complex interaction between viscosity ϵ and CL mobility

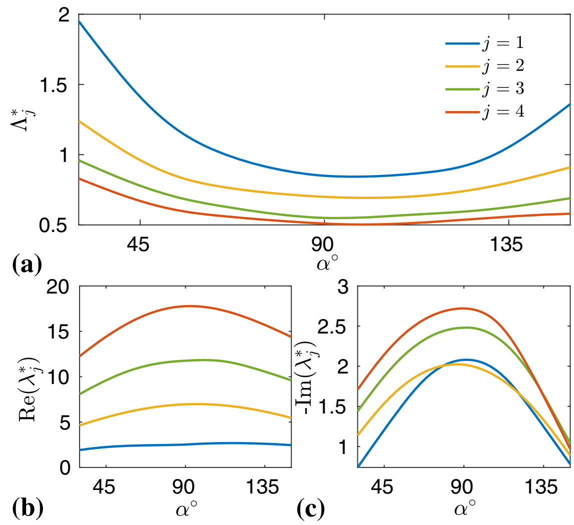

Fig. 6 **a** Critical mobility parameter Λ_j^* and corresponding **b**, **c** frequency as it depends upon contact-angle α for the first four inviscid $\epsilon = 0$ modes

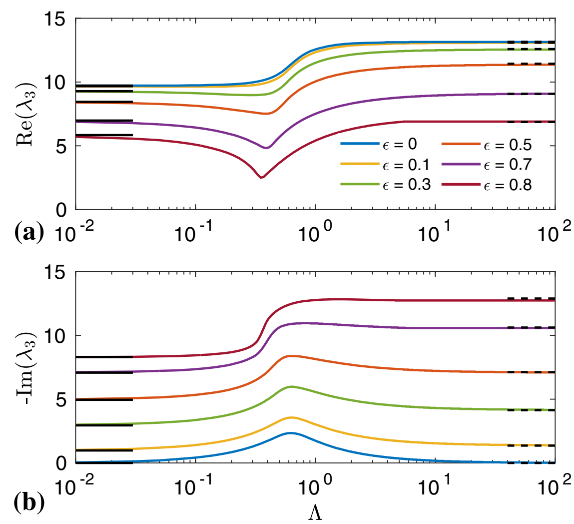

Fig. 7 Complex frequency λ_j, **a** Re(λ) and **b** Im(λ), against mobility parameter Λ for the $j = 3$ mode, as it depends upon viscosity ϵ for $\alpha = 70°$. Solid and dashed lines correspond to the free ($\Lambda = 0$) and pinned ($\Lambda = \infty$) eigenvalue solutions, respectively

Λ. When compared with the inviscid case, the decay rate Im(λ) also shows a much different dependence on Λ for larger viscosities ϵ. Figure 7b shows that for small epsilon the decay rate still has a single maximum, but as the viscosity increases that single maximum disappears, i.e., $\epsilon = 0.8$.

The computations can be validated against the analytical solution (32) for the special case $\Lambda = 0$. Figure 8 contrasts the computed and analytical frequencies λ for the first two $j = 1, 2$ resonant modes and shows an error $< 1\%$. For each mode j there is a range of ϵ where the motion is underdamped Re(λ) $\neq 0$. The transition from underdamped to overdamped motion Re(λ) $= 0$ occurs at a critical viscosity ϵ^*. For $\epsilon > \epsilon^*$, the complex solution bifurcates into two branches, as shown in Fig. 8b. Note the critical viscosity ϵ^* for $j = 2$ is smaller than that for $j = 1$, consistent with increased dissipation for higher order modes.

Figure 9 plots ϵ^* as a function of contact-angle α for free ($\Lambda = 0$, solid) and pinned ($\Lambda \to \infty$, dashed) disturbances. Note for all α, ϵ_j^* decreases with increasing mode number j, an expected result owing to the increased surface distortion for the higher modes, Fig. 3. The non-monotonic α dependence could not have been predicted a priori and presumably results from the interactions between adjacent modes.

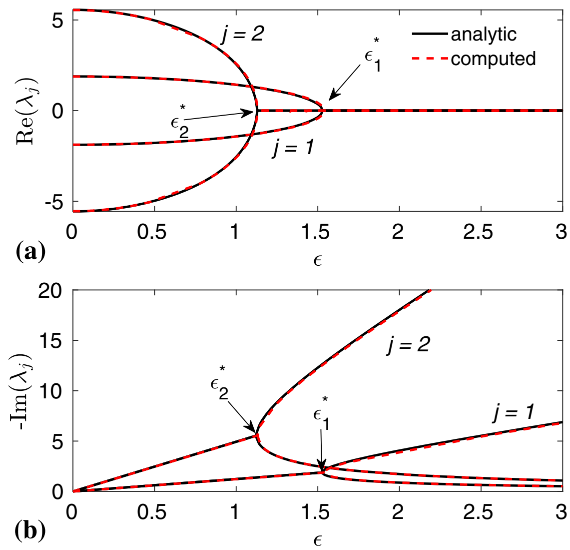

Fig. 8 Complex frequencies for the first two $j = 1, 2$ resonant modes contrasting the computed (red, dashed) and analytical (black, solid) for $\alpha = 0°$, $\Lambda = 0$. (Color figure online)

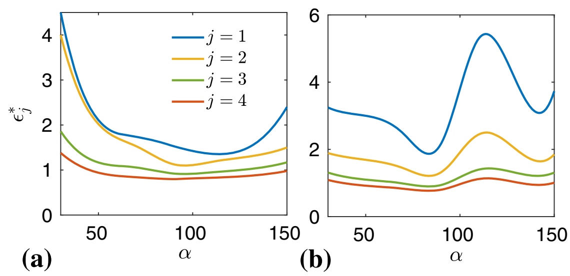

Fig. 9 Critical Ohnesorge number ϵ^* against contact-angle α for **a** free $\Lambda = 0$ and **b** pinned $\Lambda = \infty$ disturbances

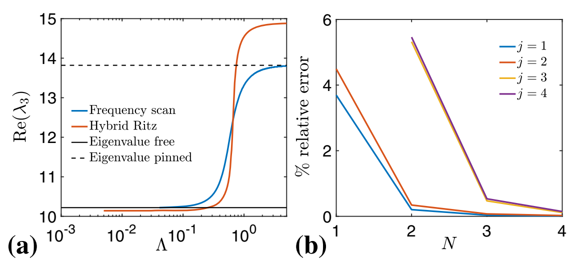

Fig. 10 **a** The third oscillatory resonant frequency as a function of Λ plotted for three different methods: the inverse eigenvalue procedure (flat black lines), the Hybrid Ritz approach (red), and the frequency scan technique introduced here. **b** Relative error for λ_{1-4} as the number N of Ritz terms is increased. All results for $\alpha = 90°$, $\epsilon = 0$. (Color figure online)

4.3 Convergence and comparisons

Several alternative techniques exist to compute fundamental frequencies. Figure 10a shows the results for three approaches for the third eigenvalue. The flat black lines represent the eigenvalue approach [24], where the free result is coincident with the analytic solution (32). As mentioned above, the eigenvalue approach fails for non-limiting Λ. Also shown is the hybrid Ritz approach, the details of which are beyond the scope of this work, though the reader can consult Bostwick and Steen [16] for holistic documentation. Unlike the eigenvalue approach, this technique considers non-limiting Λ, demonstrating the appropriate frequency shift as mobility transitions from a free to pinned CL. However, it is inconsistent with the eigenvalue approach, yielding a nearly 8% overshoot at $\Lambda \to \infty$. Also shown is our frequency scan method, which converges to the eigenvalue technique within 1% error.

Figure 10b plots relative convergence error for the first four fundamentals, as the number of Ritz terms in (25) increases from $N = 1$ to $N = 5$. The first two fundamentals for the odd and even problems are shown to be well converged, where the percent change from $N = 4$ to $N = 5$ is $< 1\%$, denoted in the plot as $N = 4$.

5 Conclusions

We have introduced a new frequency scan approach to compute the spectrum of capillary surfaces with dynamic wetting effects, characterized by a contact-line law that relates the contact-angle to contact-line speed. It is well known that for finite contact-line mobility Λ, Davis dissipation damps the oscillations even for inviscid liquids. Current techniques fail for this regime, as the eigenvalue parameter appears in the boundary condition. The proposed technique subverts this issue by treating the eigenvalue as an input forcing parameter. For this reason, the proposed technique is unique in resolving the full oscillatory and damped spectrum. The main limitation is computational expense, which only appears when identifying higher harmonics with a large damping component (larger plane to scan).

We have applied this technique to a partially wetting liquid in a rectangular channel. In doing so, we (i) verify our method, (ii) compute the oscillatory and damped spectrum, including contact-line damping, and (iii) correct a misunderstanding in the literature, namely, frequency response magnitude is not indicative of damping. The approach can be readily adapted to other interesting problems involving capillary surfaces, i.e., drops, rivulets, toroids, and liquid bridges.

Acknowledgements Professor Paul Steen passed away before this work was completed. The co-authors wish to acknowledge the invaluable contribution of Paul both to this work, as well as numerous other important problems in fluid mechanics. Paul was a brilliant scientist, who was equally creative and rigorous, and will be greatly missed by his friends, colleagues, and the fluid mechanics community.

Declarations

Conflict of interest The authors declared that they have no conflict of interest.

References

1. Cox RG (1986) The dynamics of the spreading of liquids on a solid surface. Part 1. Viscous flow. J Fluid Mech 168:169–194
2. Jiang TS, Soo-Gun OH, Slattery JC (1979) Correlation for dynamic contact angle. J Colloid Interface Sci 69(1):74–77
3. Kalliadasis S, Chang HC (1994) Apparent dynamic contact angle of an advancing gas–liquid meniscus. Phys Fluids 6(1):12–23
4. Newman S (1968) Kinetics of wetting of surfaces by polymers; capillary flow. J Colloid Interface Sci 26:209–213
5. Shikhmurzaev YD (2008) Capillary flows with forming interfaces. Chapman & Hall, Boca Raton
6. Bracke M, Voeght F, Joos P (1989) The kinetics of wetting: the dynamic contact angle. Prog Colloid Polym Sci 79:142–149
7. Fries N, Dreyer M (2008) The transition from inertial to viscous flow in capillary rise. J Colloid Interface Sci 327(1):125–128
8. Kistler SF (1993) Wettability. In: Berg J (ed) Wettability. Marcel Dekker, New York, p 311
9. Šikalo Š, Wilhelm HD, Roisman IV, Jakirlić S, Tropea C (2005) Dynamic contact angle of spreading droplets: experiments and simulations. Phys Fluids 17(6):1–13
10. Saha AA, Mitra SK (2009) Effect of dynamic contact angle in a volume of fluid (VOF) model for a microfluidic capillary flow. J Colloid Interface Sci 339(2):461–480
11. Hocking LM (1987) The damping of capillary-gravity waves at a rigid boundary. J Fluid Mech 179:253–266
12. Davis SH (1980) Moving contact lines and rivulet instabilities. Part 1. The static rivulet. J Fluid Mech 98(2):225–242
13. McCraney J, Weislogel M, Steen P (2020) OpenFOAM simulations of late stage container draining in microgravity. Fluids 5(4):207
14. Jenson RM, Weislogel MM, Klatte J, Dreyer ME (2010) Dynamic fluid interface experiments aboard the international space station: model benchmarking dataset. J Spacecr Rockets 47(4):670–679
15. Wölk G, Dreyer M, Rath HJ, Weislogel MM (1997) Damped oscillations of a liquid/gas surface upon step reduction in gravity. J Spacecr Rockets 34(1):110–117
16. Bostwick JB, Steen PH (2014) Dynamics of sessile drops. Part 1. Inviscid theory. J Fluid Mech 760:5–38
17. Bostwick JB, Steen PH (2015) Stability of constrained capillary surfaces. Annu Rev Fluid Mech 47(May):539–568
18. Prosperetti A (1977) Viscous effects on perturbed spherical flows. Q Appl Math 34:339–352

19. Prosperetti A (1980) Normal-mode analysis for the oscillations of a viscous liquid drop in an immiscible liquid. J Mech 19:149–182
20. Joseph DD (2003) Viscous potential flow. J Fluid Mech 479(479):191–197
21. Joseph DD (2006) Helmholtz decomposition coupling rotational to irrotational flow of a viscous fluid. Proc Natl Acad Sci USA 103(39):14272–14277
22. Lyubimova DV, Lyubimova TP, Shklyaev SV (2004) Non-axisymmetric oscillations of a hemispherical drop. Fluid Dyn 39(6):851–862
23. Steen PH, Chang CT, Bostwick JB (2019) Droplet motions fill a periodic table. Proc Natl Acad Sci USA 116(11):4849–4854
24. Bostwick JB, Steen PH (2018) Static rivulet instabilities: varicose and sinuous modes. J Fluid Mech 837:819–838
25. Bostwick JB, Steen PH (2013) Coupled oscillations of deformable spherical-cap droplets. Part 2. Viscous motions. J Fluid Mech 714:336–360
26. Bostwick JB, Steen PH (2009) Capillary oscillations of a constrained liquid drop. Phys Fluids 21(3):032108
27. Bostwick JB, Steen PH (2010) Stability of constrained cylindrical interfaces and the torus lift of Plateau–Rayleigh. J Fluid Mech 647:201–219
28. Strani M, Sabetta F (1984) Free vibrations of a drop in partial contact with a solid support. J Fluid Mech 141:233–247
29. Lyubimov DV, Lyubimova TP, Cherepanov AA (2020) Resonance oscillations of a drop (bubble) in a vibrating fluid. J Fluid Mech 909:A18
30. Benjamin TB, Scott JC (1979) Gravity-capillary waves with edge constraints. J Fluid Mech 92(2):241–267
31. Graham-Eagle J (1983) A new method for calculating eigenvalues with applications to gravity-capillary waves with edge constraints. Math Proc Camb Philos Soc 94:553–564
32. Prosperetti A (2012) Linear oscillations of constrained drops, bubbles, and plane liquid surfaces. Phys Fluids 24(3):03219
33. Bostwick JB, Steen PH (2013) Coupled oscillations of deformable spherical-cap droplets. Part 1. Inviscid motions. J Fluid Mech 714:312–335
34. Benjamin T, Ursell F (1954) The stability of the plane free surface of a liquid in vertical periodic motion. Proc R Soc Lond 225(1163):505–515
35. Bostwick JB, Steen PH (2016) Response of driven sessile drops with contact-line dissipation. Soft Matter 12(43):8919–8926
36. Chang CT, Bostwick J, Daniel S, Steen P (2015) Dynamics of sessile drops. Part 2. Experiment. J Fluid Mech 768:442–467
37. Kreyszig E (1991) Differential geometry. Dover, Mineola
38. Walter J (1973) Regular eigenvalue problems with eigenvalue parameter in the boundary condition. Math Z 133(4):301–312
39. Kopachevskii N (1972) Hydrodynamics in weak gravitational fields two-dimensional oscillations of an ideal fluid in a rectangular channel. Fluid Dyn 7:705–714
40. Lyubimov DV, Lyubimova TP, Shklyaev SV (2006) Behavior of a drop on an oscillating solid plate. Phys Fluids 18(1):012101
41. Ludwicki JM, Robinson FL, Steen PH (2020) Switchable wettability for condensation heat transfer. ACS Appl Mater Interfaces 12(19):22115–22119
42. Davis CS, Crosby AJ (2011) Mechanics of wrinkled surface adhesion. Soft Matter 7(11):5373–5381
43. Al Bitar L, Voigt D, Zebitz CP, Gorb SN (2010) Attachment ability of the codling moth *Cydia pomonella* L. to rough substrates. J Insect Physiol 56(12):1966–1972
44. Autumn K, Liang YA, Hsieh ST, Zesch W, Chan WP, Kenny TW, Fearing R, Full RJ (2000) Adhesive force of a single gecko foot-hair. Nature 405(6787):681–685
45. Barthlott W, Neinhuis C (1997) Purity of the sacred lotus, or escape from contamination in biological surfaces. Planta 202(1):1–8
46. Manakasettharn S, Ashley Taylor J, Krupenkin TN (2011) Bio-inspired artificial iridophores based on capillary origami: fabrication and device characterization. Appl Phys Lett 99(14):97–100
47. Castrejón-Pita JR, Baxter WR, Morgan J, Temple S, Martin GD, Hutchings IM (2013) Future, opportunities and challenges of inkjet technologies. At Sprays 23(6):571–595
48. Fontelos M, Kindelan U (2008) The shape of charged drops over a solid surface and symmetry-breaking instabilities. SIAM J Appl Math 69(1):126–148
49. Krupenkin T, Taylor JA (2011) Reverse electrowetting as a new approach to high-power energy harvesting. Nat Commun 2(1):1–8